Special Section — Marine Controlled-Source Electromagnetic Methods

Rigorous 3D inversion of marine CSEM data based on the integral equation method

Alexander Gribenko[1] and Michael Zhdanov[1]

ABSTRACT

Marine controlled-source electromagnetic (MCSEM) surveys have become an important part of offshore petroleum exploration. However, due to enormous computational difficulties with full 3D inversion, practical interpretation of MCSEM data is still a very challenging problem. We present a new approach to 3D inversion of MCSEM data based on rigorous integral-equation (IE) forward modeling and a new IE representation of the sensitivity (Fréchet derivative matrix) of observed data to variations in sea-bottom conductivity. We develop a new form of the quasi-analytical approximation for models with variable background conductivity (QAVB) and apply this form for more efficient Fréchet derivative calculations. This approach requires just one forward modeling on every iteration of the regularized gradient-type inversion algorithm, which speeds up the computations significantly. We also use a regularized focusing inversion method, which provides a sharp boundary image of the petroleum reservoir. The methodology is tested on a 3D inversion of the synthetic EM data representing a typical MCSEM survey conducted for offshore petroleum exploration.

INTRODUCTION

During recent years, marine controlled-source electromagnetic (MCSEM) surveys have become intensively used for offshore petroleum exploration (Eidesmo et al., 2002; Ellingsrud et al., 2002; Tompkins, 2004; Carazzone et al., 2005; Hesthammer and Boulaenko, 2005; Srnka et al., 2005). The success of the EM method's application for the search of oil and gas reservoirs is based on the fundamental fact that oil- and gas-containing structures are characterized by very high resistivity, while the surrounding sea-bottom formations filled with salt water are very conductive. Therefore, a petroleum reservoir represents a clear target for EM methods. However, the interpretation of MCSEM data is still a very challenging problem, especially if one would like to take into account a real 3D structure of a sea-bottom geologic formation. The inversion of MCSEM data is complicated by the fact that the EM response of a petroleum reservoir is very weak in comparison with a background EM field generated by an electric dipole transmitter in layered geoelectrical structures formed by a conductive seawater layer and bottom sediments.

There were several publications recently reporting significant progress in 3D inversion of MCSEM data based on the finite-difference (FD) method (Newman and Boggs, 2004; Hoversten et al., 2004, 2005). In this paper, we present a different approach to 3D inversion of MCSEM data, which uses a rigorous integral-equation-(IE) based forward modeling and regularized focusing inversion algorithm. There are several advantages in using the IE method in the MCSEM data inversion in comparison with the more traditional FD approach. First, IE forward modeling requires the calculation of the Green's tensors for the background conductivity model. These tensors can be precomputed only once and saved for multiple use on every iteration of inversion, which speeds up the computation of the predicted data on each iteration significantly. Second, the same precomputed Green's tensors can be readily used for Fréchet derivative calculations, which is another important element of inversion. Finally, IE forward modeling and inversion requires the discretization of the domain of inversion only, while in the framework of the FD method, one has to discretize the entire modeling domain, which includes not only the area of investigation but an additional domain surrounding this area (including the areas in the air). As a result, the IE inversion method requires just one forward modeling on every iteration step, which speeds up the computations and results in a relatively fast but rigorous inversion method. To obtain a stable solution of a 3D inverse problem, we apply a regularization method based on a focusing stabilizing functional (Zhdanov, 2002). This stabilizer

helps generate a sharp and focused image of ous conductivity distribution, which is important in petroleum exploration with the goal of delineating the boundaries of a prospective reservoir.

We present the results of the application of the rigorous inversion method to the interpretation of synthetic MCSEM data.

INTEGRAL EQUATION METHOD IN 3D INVERSION OF MCSEM DATA

We consider first, the typical MCSEM survey consisting of a set of sea-bottom electrical and magnetic receivers and a horizontal electric dipole transmitter towing at some elevation above the sea bottom. This type of survey is often referred to as sea bed logging, SBL (Eidesmo et al., 2002). The transmitter generates a frequency-domain EM field. The operating frequencies are usually selected to be low enough (in a range of 0.1–5 Hz) to propagate through the conductive seawater and sea-bottom layers of the sediments and to illuminate the sea-bottom geologic structures. The field recorded by the receivers can be represented as a sum of the normal EM field, $\{\mathbf{E}^{norm}, \mathbf{H}^{norm}\}$, generated in a horizontally layered background model formed by seawater and sediment layers, and an anomalous part, $\{\mathbf{E}^a, \mathbf{H}^a\}$, related to the horizontal conductivity inhomogeneities $\Delta\sigma$ present in the sea bottom:

$$\mathbf{E} = \mathbf{E}^{norm} + E^a, \quad \mathbf{H} = \mathbf{H}^{norm} + \mathbf{H}^a.$$

The anomalous electromagnetic field is related to the electric current induced in the inhomogeneity $\mathbf{j} = \Delta\sigma\mathbf{E}$, according to the following integral formulas:

$$\mathbf{E}^a(\mathbf{r}_j) = \int\int\int_D \hat{\mathbf{G}}_E(\mathbf{r}_j|\mathbf{r}) \cdot [\Delta\sigma(\mathbf{r})\mathbf{E}(\mathbf{r})]dv = \mathbf{G}_E[\Delta\sigma\mathbf{E}],$$

$$\tag{1}$$

$$\mathbf{H}^a(\mathbf{r}_j) = \int\int\int_D \hat{\mathbf{G}}_H(\mathbf{r}_j|\mathbf{r}) \cdot [\Delta\sigma(\mathbf{r})\mathbf{E}(\mathbf{r})]dv = \mathbf{G}_H[\Delta\sigma\mathbf{E}],$$

$$\tag{2}$$

where $\hat{\mathbf{G}}_E(\mathbf{r}_j|\mathbf{r})$ and $\hat{\mathbf{G}}_H(\mathbf{r}_j|\mathbf{r})$ are the electric and magnetic Green's tensors defined for an unbounded conductive medium with the normal (horizontally layered) conductivity σ_{norm}; $\mathbf{G}_E$ and $\mathbf{G}_H$ are corresponding Green's linear operators; and domain D represents a volume with the anomalous conductivity distribution $\sigma(\mathbf{r}) = \sigma_{norm} + \Delta\sigma(\mathbf{r}), \mathbf{r} \in D$.

We use integral equations 1 and 2 to formulate both the forward and inverse problems of the SBL method. Indeed, in short form these equations can be written as

$$\mathbf{d} = A(\Delta\sigma),$$

$$\tag{3}$$

where A is a forward modeling operator, $\mathbf{d}$ stands for the observed EM data in the sea-bottom receivers, and $\Delta\sigma$ is a vector formed by the anomalous conductivities within the targeted domain. The inversion is based on minimization of the Tikhonov parametric functional $P^\alpha(\Delta\sigma)$, with the corresponding stabilizer $s(\Delta\sigma)$ (Tikhonov and Arsenin, 1977):

$$P^\alpha(\Delta\sigma) = \|\mathbf{W}_d(A(\Delta\sigma) - \mathbf{d})\|^2_{L_2} + \alpha s(\Delta\sigma),$$

$$\tag{4}$$

where $\mathbf{W}_d$ is the data-weighting matrix, and α is a regularization parameter.

There are several possible choices for the stabilizer (Zhdanov, 2002). In this paper, we use two of them:

1) The minimum norm stabilizer (s_{MN}), which is equal to the square L_2 norm of the difference between the current model $\Delta\sigma$ and an appropriate a priori model $\Delta\sigma_{apr}$:

$$s_{MN}(\Delta\sigma) = \|\mathbf{W}_m(\Delta\sigma - \Delta\sigma_{apr})\|^2_{L_2},$$

where $\mathbf{W}_m$ is the weighting matrix of the model parameters.

2) The minimum support stabilizer (s_{MS}), which is proportional to the volume (support) of the nonzero values of the difference between the current model $\Delta\sigma$ and the a priori model $\Delta\sigma_{apr}$:

$$s_{MS}(\Delta\sigma) = \int\int\int_D \frac{(\Delta\sigma - \Delta\sigma_{apr})^2}{(\Delta\sigma - \Delta\sigma_{apr})^2 + e^2}dv, \quad (5)$$

where e is the focusing parameter.

It was shown by Portniaguine and Zhdanov (1999) that the minimum support functional minimizes the volume of nonzero parameter distribution (minimizes the support of the inverse model), if e tends to zero: $e \to 0$. The principles of the optimal focusing parameter selection are discussed in Zhdanov and Tolstaya (2004).

The most common approach to minimization of the parametric functional $P(\Delta\sigma)$ is based on using gradient-type methods. For example, the regularized conjugate gradient (RCG) algorithm of the parametric functional minimization in the case of the minimum norm stabilizer can be summarized as follows (Zhdanov, 2002):

$$\mathbf{r}_n = A(\Delta\sigma_n) - \mathbf{d}, \quad \mathbf{l}_n = \mathbf{l}(\Delta\sigma_n) = \mathrm{Re}\mathbf{F}_n^\star\mathbf{W}_d^\star\mathbf{W}_d\mathbf{r}_n$$
$$+ \alpha\mathbf{W}_m^\star\mathbf{W}_m(\Delta\sigma_n - \Delta\sigma_{apr}), \tag{6a}$$

$$\beta_n = \|\mathbf{l}_n\|^2/\|\mathbf{l}_{n-1}\|^2, \quad \tilde{\mathbf{l}}_n = \mathbf{l}_n + \beta_n\tilde{\mathbf{l}}_{n-1}, \quad \tilde{\mathbf{l}}_0 = \mathbf{l}_0, \tag{6b}$$

$$k_n = (\tilde{\mathbf{l}}_n, \mathbf{l}_n)/\{\|\mathbf{W}_d\mathbf{F}_n\tilde{\mathbf{l}}_n\|^2 + \alpha\|\mathbf{W}_m\tilde{\mathbf{l}}_n\|^2\}, \tag{6c}$$

$$\Delta\sigma_{n+1} = \Delta\sigma_n - k_n\tilde{\mathbf{l}}_n, \tag{6d}$$

where $\mathbf{r}_n$ is a residual at the iteration step n, $\mathbf{l}_n$ is the gradient direction, $\mathbf{F}_n$ is a Fréchet derivative matrix, $\mathbf{W}_d$ is a data weighting matrix, α is a regularization parameter, $\mathbf{W}_m$ is a model weighting matrix, $\tilde{\mathbf{l}}_n$ is the conjugate direction, k_n is a length of the iteration step, $\|\ \|$ denotes vector or matrix norm, and * sign represents adjoint matrix.

The appropriate selection of the data and model parameters weighting matrices is very important for the success of the inversion. We determine the data weights as a diagonal matrix formed by the inverse absolute values of the normal field. Computation of the model weighting matrix is based on sensitivity analysis. In this research, we select as the square root of the sensitivity matrix in the initial model:

$$\mathbf{W}_m = \sqrt{\mathbf{diag}(\mathbf{F}_0^\star\mathbf{F}_0)^{1/2}}. \tag{7}$$

As a result, we obtain a uniform sensitivity of the data to different model parameters (Zhdanov, 2002).

In the case of the minimum support stabilizer we use the reweighted regularized conjugate gradient (RRCG) method introduced in Zhdanov (2002, pp. 161–166). This algorithm is similar to the RCG algorithm represented by equation 6. However, the inversion is conducted in the space of the weighted model parameters $\mathbf{m}_n^w$, which are related to the original parameters by the formula:

$$\mathbf{m}_n^w = \mathbf{W}_m \widetilde{\mathbf{W}}_{en} \widetilde{\mathbf{m}}_n, \qquad (8)$$

where the reweighting matrix $\bar{\mathbf{W}}_{en}$ is equal to

$$\widetilde{\mathbf{W}}_{en} = \{\mathbf{diag}[(\widetilde{\mathbf{m}}_n^2 + e^2)^{1/2}]\}^{-1}. \qquad (9)$$

We refer the interested readers to a book on inversion theory by Zhdanov (2002) for in-depth explanation of the RRCG technique, which is widely used in different geophysical applications.

In expressions 8 and 9 we use the logarithmic model parameters, vector $\widetilde{\mathbf{m}}$, with the scalar components $\widetilde{m}_i$, given by the formula:

$$\widetilde{m}_i = \ln\left(\frac{\Delta\sigma_i - \Delta\sigma_i^-}{\Delta\sigma_i^+ - \Delta\sigma_i}\right). \qquad (10)$$

This log parameterization has a property that the scalar components of the original conductivity vector $\Delta\boldsymbol{\sigma}$ always remain within the given lower and upper bounds, $\Delta\sigma_i^-$ and $\Delta\sigma_i^+$, respectively:

$$\Delta\sigma_i^- \leq \Delta\sigma_i \leq \Delta\sigma_i^+, \quad i = 1,2,\dots. L. \qquad (11)$$

We apply the adaptive regularization method. The regularization parameter α is updated in the process of the iterative inversion as follows:

$$\alpha_n = \alpha_1 q^{n-1}; \quad n = 1,2,3 \dots \dots; \quad 0 < q < 1. \qquad (12)$$

In order to avoid divergence, we begin an iteration from a value of α_1, which can be obtained as a ratio of the misfit functional and the stabilizer for an initial model, then reduce α_n according to formula 12 on each subsequent iteration and continuously iterate until the misfit condition is reached:

$$r_{n0}^w = \|\mathbf{r}_{n0}^w\| = \|\mathbf{W}_d(\mathbf{A}(\mathbf{m}_{\alpha_{n0}}) - \mathbf{d})\|/\|\mathbf{W}_d\mathbf{d}\| \leq \delta, \quad (13)$$

where r_{n0}^w is the normalized weighted residual, and δ is the relative level of noise in the weighted observed data.

Parameter q controls the rate of decrease of the regularization parameter α_n in the process of inversion. This parameter is usually selected within an interval $[0.5; 0.9]$.

Note that in practical applications of the regularized iterative inversion, we begin the inverse process with the minimum norm (smooth) inversion to produce an initial image of the target. After a few minimum norm iterations we switch the iterative process to the minimum support inversion by introducing a reweighting matrix $\bar{\mathbf{W}}_{en}$ (equation 9) and continue with the focusing inversion until the misfit functional reaches the required misfit level. In other words, the developed algorithm has the flexibility to run the minimum norm inversion to produce a smooth image of the target, or to run a combination of the smooth and focusing inversions to generate a more focused image. Examples of practical applications of this approach will be given below in a section on synthetic MCSEM data inversion.

Formula 6 demonstrates that every iteration step requires at least one forward modeling solution to find the predicted data $A(\Delta\boldsymbol{\sigma}_n)$. Additional computations are needed to find the Fréchet derivative $\mathbf{F}_n$, and the optimal length of the iteration step k_n.

Thus, the critical element of the inversion is computing the Fréchet derivative of the forward modeling operator. Direct computation of the Fréchet derivative is very time consuming even when the reciprocity principle is utilized. It was demonstrated by Golubev

and Zhdanov (2005) for MT data inversion, that the number of forward modelings can be reduced to one on every iteration step if we compute the Fréchet derivative using the modified form of the quasi-analytical (QA) approximation (Zhdanov et al., 2000). In the current paper, we develop a new form of the QA approximation for models with variable background conductivity (QAVB) and apply this form for more efficient Fréchet derivative calculations. We use this approach for developing a fast and rigorous method of the MCSEM data inversion. This method uses IE-based forward modeling solvers on every iteration of the RRCG inversion to calculate the predicted data. That is why it delivers a rigorous inversion. At the same time, to speed up the computations, the method uses the QAVB approximation for the Fréchet derivative calculation. We will discuss the principles of the new method of Fréchet derivative calculation using QAVB approximation in the next section.

Another important element of the IE-based inversion is the selection of the appropriate background conductivity model. This problem is a typical one in many methods of exploration geophysics. There exist several different techniques for solving this problem. The simplest approach is based on 1D inversion of the observed data set using the same regularized conjugate gradient method, described above. One can use the corresponding 1D inverse model as a background model for the subsequent 3D inversion. We can also find the 1D background conductivity by 1D inversion of the data in the receivers located outside of the area with the target. We will present an example of such an approach in our numerical study below.

FRÉCHET DERIVATIVE CALCULATION USING QUASI-ANALYTICAL APPROXIMATION FOR A VARIABLE BACKGROUND (QAVB)

We assume now that the conductivity within a 3D geoelectrical model can be represented by the normal (horizontally layered) conductivity σ_{norm}, background conductivity $\sigma_b = \sigma_{\text{norm}} + \Delta\sigma_b$, and an arbitrarily varying conductivity $\sigma = \sigma_b + \Delta\sigma_a$, within a domain D.

In this model, the electromagnetic field can be presented as a sum of the background field, $\mathbf{E}^b, \mathbf{H}^b$, and the anomalous field, $\mathbf{E}^{\Delta\sigma_a}, \mathbf{H}^{\Delta\sigma_a}$:

$$\mathbf{E} = \mathbf{E}^b + \mathbf{E}^{\Delta\sigma_a}, \quad \mathbf{H} = \mathbf{H}^b + \mathbf{H}^{\Delta\sigma_a},$$

where the background field is a field generated by the given sources in the model with a background distribution of conductivity σ_b, and the anomalous field is produced by the anomalous conductivity distribution $\Delta\sigma_a$.

In Appendix A, we introduce a new form of quasi-analytical approximation of the anomalous EM field for a variable background (QAVB):

$$\mathbf{E}_{QAVB}^a(\mathbf{r}_j) = \int\int\int_D \hat{\mathbf{G}}_E(\mathbf{r}_j|\mathbf{r}) \cdot \left[\frac{\Delta\sigma_a(\mathbf{r})}{1 - g^Q(\mathbf{r})}\mathbf{E}^b(\mathbf{r})\right]dv,$$

$$(14)$$

and

$$\mathbf{H}_{QAVB}^a(\mathbf{r}_j) = \int\int\int_D \hat{\mathbf{G}}_H(\mathbf{r}_j|\mathbf{r}) \cdot \left[\frac{\Delta\sigma_a(\mathbf{r})}{1 - g^Q(\mathbf{r})}\mathbf{E}^b(\mathbf{r})\right]dv,$$

$$(15)$$

where:

$$g^Q(\mathbf{r}) = \frac{\mathbf{E}^Q(\mathbf{r}) \cdot \mathbf{E}^{b*}(\mathbf{r})}{\mathbf{E}^b(\mathbf{r}) \cdot \mathbf{E}^{b*}(\mathbf{r})}, \qquad (16)$$

and $\mathbf{E}^Q$ is the quasi-Born approximation of the anomalous electric field:

$$\mathbf{E}^Q = \mathbf{G}_E[\Delta\sigma_a \mathbf{E}^b].$$

The main difference between the QAVB and the original QA approximation can be explained as follows. It is very well known that the accuracy of any approximation of the anomalous EM field depends on the value of the anomalous conductivity. The smaller the anomalous conductivity is, the more accurate the approximate solutions are (Zhdanov, 2002). In the case of the original QA approximation, the anomalous field is caused by an anomalous conductivity, which is the difference between the total conductivity of the model and some known layered-earth background model. In the case of the QAVB approximation, the anomalous field is caused by an anomalous conductivity, which is calculated as a difference between the total conductivity and some arbitrary inhomogeneous background conductivity: $\Delta\sigma_a = \sigma - \sigma_b$. In principle, this background conductivity σ_b can be selected very close to the total conductivity, which results in a very small value of the anomalous conductivity and a high accuracy of the QAVB approximation.

Another advantage of using expressions 14 and 15, as mentioned in Zhdanov and Hursán (2000), is the ability to generate a simple formula for the Fréchet derivative operator which can be used in inversion algorithms. For example, by introducing a perturbation of the anomalous conductivity $\delta\Delta\sigma_a(\mathbf{r})$, we can calculate the corresponding perturbation of the electric field $\delta\mathbf{E}(\mathbf{r}_j)$ on the basis of equation 14. After some straightforward algebra, we arrive at the following integral representations for the Fréchet derivative of the electric and magnetic fields:

$$\left.\frac{\partial\mathbf{E}(\mathbf{r}_j)}{\partial\Delta\sigma_a(\mathbf{r})}\right|_{\Delta\sigma_a} = \mathbf{F}_E(\mathbf{r}_j|\mathbf{r}), \qquad \left.\frac{\partial\mathbf{H}(\mathbf{r}_j)}{\partial\Delta\sigma_a(\mathbf{r})}\right|_{\Delta\sigma_a} = \mathbf{F}_H(\mathbf{r}_j|\mathbf{r}),$$

$$(17)$$

where the vector functions $\mathbf{F}_E$ and $\mathbf{F}_H$ are the kernels of the integral Fréchet derivative operators:

$$\mathbf{F}_{E,H}(\mathbf{r}_j|\mathbf{r}) = \left[\frac{1}{1 - g^Q(\mathbf{r})}\hat{\mathbf{G}}_{E,H}(\mathbf{r}_j|\mathbf{r}) + \hat{\mathbf{K}}(\mathbf{r}_j|\mathbf{r})\right]\mathbf{E}^b(\mathbf{r}),$$

$$(18)$$

and

$$\hat{\mathbf{K}}(\mathbf{r}_j|\mathbf{r}) = \iiint_D \frac{\Delta\sigma_a(\mathbf{r}')}{(1 - g^Q(\mathbf{r}'))^2}\hat{\mathbf{G}}_E(\mathbf{r}_j|\mathbf{r}') \cdot \mathbf{E}^b(\mathbf{r}')$$
$$\times \left[\frac{\mathbf{E}^{b*}(\mathbf{r}')}{\mathbf{E}^b(\mathbf{r}') \cdot \mathbf{E}^{b*}(\mathbf{r}')} \cdot \hat{\mathbf{G}}_E(\mathbf{r}'|\mathbf{r})\right]dv'. \qquad (19)$$

Function g^Q is determined by expression 16.

We can use expressions 17-19 for computing the Fréchet derivatives required by the RCG algorithm 6. Indeed, we can treat the electric field $\mathbf{E}^{(n)}$ found on iteration number n as a background field $\mathbf{E}^b$ for a subsequent iteration $(n + 1)$, $\mathbf{E}^b = \mathbf{E}^{(n)}$. In this case, the Fréchet derivative at iteration number n can be found by direct integration

from expressions 17-19 involving the electric field $\mathbf{E}^{(n)}$ computed on the current iteration:

$$\mathbf{F}_{E,H}(\mathbf{r}_j|\mathbf{r}) = \left[\frac{1}{1 - g^Q(\mathbf{r})}\hat{\mathbf{G}}_{E,H}(\mathbf{r}_j|\mathbf{r}) + \hat{\mathbf{K}}(\mathbf{r}_j|\mathbf{r})\right]\mathbf{E}^{(n)}(\mathbf{r}),$$

$$(20)$$

and

$$\hat{\mathbf{K}}(\mathbf{r}_j|\mathbf{r}) = \iiint_D \frac{\Delta\sigma_n(\mathbf{r}')}{(1 - g^Q(\mathbf{r}'))^2}\hat{\mathbf{G}}_E(\mathbf{r}_j|\mathbf{r}') \cdot \mathbf{E}^{(n)}(\mathbf{r}')$$
$$\times \left[\frac{\mathbf{E}^{(n)*}(\mathbf{r}')}{\mathbf{E}^{(n)}(\mathbf{r}') \cdot \mathbf{E}^{(n)*}(\mathbf{r}')} \cdot \hat{\mathbf{G}}_E(\mathbf{r}'|\mathbf{r})\right]dv'. \quad (21)$$

Note that the electric field $\mathbf{E}^{(n)}$ is computed, as a rule, using the rigorous IE forward-modeling method. However, to speed up the computations, different numerical techniques can be used, as will be discussed below in the section on numerical examples. We use systematically the QAVB approximation for computing the Fréchet derivatives, based on formulas 20 and 21. As we can see, in the inversion algorithm, the background field required by the QAVB approximation is equal to the predicted electric field found on the previous iteration. Therefore, no extra computation is required to find the background field for the Fréchet derivative calculation. The corresponding numerical method of the Fréchet derivative computations is based on the discrete form of the explicit integral expressions 20 and 21, which simplifies all calculations dramatically. However, similar to conventional inversion techniques, we do not need to keep the entire Fréchet derivative matrix in the computer memory. We save the results of the application of the adjoint Fréchet matrix to the weighted residual field, $\mathbf{F}_n^* \mathbf{W}_d^* \mathbf{W}_d \mathbf{r}_n$, only. The major difference between the conventional approach and our approach is that in the first case, one has to solve the full 3D EM forward problem on every iteration of the inversion in order to find the term $\mathbf{F}_n^* \mathbf{W}_d^* \mathbf{W}_d \mathbf{r}_n$. In our method, we do not need to solve any forward problem to find the Fréchet derivative, because we compute this term by direct algebraic expression arising from our new integral representation of the Fréchet matrix. The same algebraic expression is used to find the optimal length of the iteration step according to expression 6c. As a result, our new inversion technique, based on the IE method, requires just one forward modeling on every iteration step without any extra memory usage, while the conventional inversion schemes require, as a rule, at least three forward modeling solutions per inversion iteration (one to compute the predicted data, another one to compute the gradient direction, and the last one for optimal calculation of the iteration step). This approach results in a very efficient inversion method.

SYNTHETIC MCSEM DATA INVERSION

We have investigated several models of marine CSEM surveys. First, we have considered a 2D CSEM survey, which is currently the most widely used in offshore exploration. The typical 2D survey consists of a set of receivers located along a line at the sea bottom and of an electric bipole transmitter towed parallel to and above the receivers.

Model 1

In the first set of numerical experiments, we assume that a synthetic CSEM survey is conducted in relatively shallow water with a sea

depth of 300 m (Figure 1). The survey consists of seventeen sea-bottom receivers and an electric dipole transmitter moving along a line passing directly above the receivers at an elevation of 50 m above the sea bottom. The separation between the receivers is 1000 m. The transmitter generates a frequency-domain EM field with two frequencies of 0.25 and 0.75 Hz from points every 200 m along the transmitter line. The maximum transmitter-receiver offset is 10 km. The background geoelectrical model consists of a seawater layer with a thickness of 300 m and a resistivity of 0.25 ohm-m, a sea-bottom gas-hydrate layer with a thickness of 100 m and a resistivity of 5 ohm-m, conductive sea-bottom sediments with a thickness of 1400 m and a resistivity of 1 ohm-m, and a more resistive basement with a resistivity of 3.33 ohm-m (Figure 1). We assume that we have two petroleum reservoirs with the same thickness of 100 m and a resistivity of 50 ohm-m, but located at depths of 1300 and 1000 m, respectively, below sea level (Figure 1). The horizontal dimensions of the reservoirs are 2 and 1 km in the x-direction and 1.8 km in the y-direction, respectively.

The synthetic CSEM data were computed for this model using the rigorous IE method. We use as input data for the inversion the total electric field E_x, normalized by the absolute value of the normal electric field E_x^{norm}, generated in the horizontally layered background model described above.

First, we applied the rigorous inversion algorithm to the inversion of the noise-free synthetic CSEM data computed for this model. The area of inversion is extended from $-4,000$ to $4,000$ m in the x-direction, from -900 to 900 m in the y-direction, and from 800 to $1,600$ m at a depth with cell sizes equal to 500, 600, and 50 m in the x-, y-, and z-directions, respectively.

We ran 30 iterations of the minimum norm (smooth) inversion and 53 iterations of the focusing inversion. No a priori model was used in the inversion. The convergence plot is shown in Figure 2 shows the normalized residual versus the iteration number. Figure 2b presents the normalized parametric functional behavior. The normalized residual is computed by the formula:

$$r_n^w = \|\mathbf{W}_d(\mathbf{A}(\mathbf{m}_{\alpha_{n0}}) - \mathbf{d})\|/\|\mathbf{W}_d\mathbf{d}\|, \qquad (22)$$

where the data-weighting matrix is a diagonal matrix formed by the inverse absolute values of the background electric field.

Note that the first iteration of the RRCG method is computed with the regularization parameter $\alpha = 0$. After about 50 iterations of the rigorous inversion, the normalized residual reaches 3%. Figure 3 shows a vertical section of the inversion result. As one can see, the depth and the horizontal extent of both reservoirs are recovered well in the inverse image.

In the next numerical experiment, we contaminated the synthetic observed data with random Gaussian noise. The noise level increases linearly from 1% at zero offset up to 7% at 10,000 m offset to simulate a typical noise behavior in the field data.

The normalized inline electric field data recorded in receiver 10($x = 1000$ m) for two frequencies are shown in Figures 4 and 5. We plot here the real and imaginary parts of the total electric field E_x, normalized by the absolute values of the normal electric field E_x^{norm}, generated in the horizontally layered background model formed by the seawater, the sea-bottom gas-hydrate layer, the conductive sea-bottom sediments, and a relatively resistive basement. One can see rather complex anomalous behavior of the observed field. We have applied our inversion algorithm to the noisy data. We should note that we use 3D forward modeling and inversion to process the data observed by this 2D synthetic survey. In order to speed up the computations in this example, we have used the multigrid quasi-linear (MGQL) forward modeling code to compute the pre-
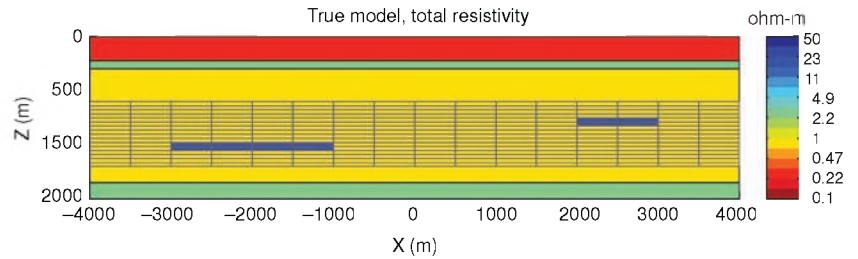

Figure 1. Model 1 formed by two resistive reservoirs located at different depths. The area shown with grids defines the extent of the anomalous domain in the inversions.
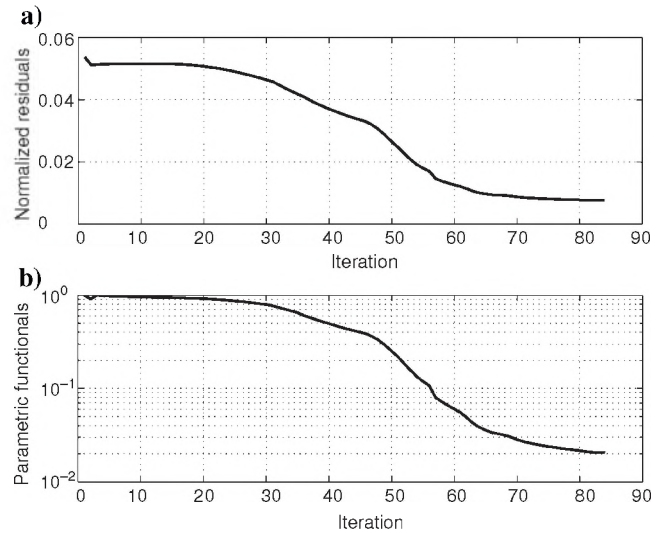

Figure 2. The convergence plots of the iterative inversion for Model 1. (a) The normalized residual versus the iteration number, (b) the normalized parametric functional behavior.
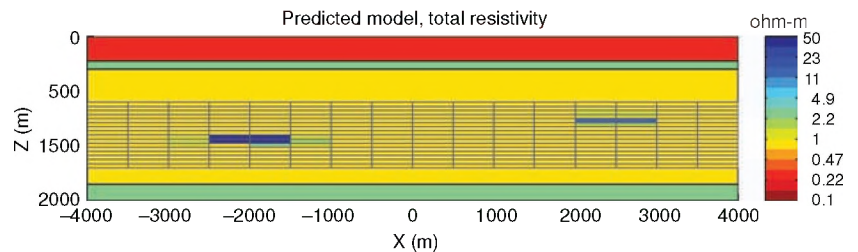

Figure 3. The vertical section of the result of the inversion of the noise-free data for Model 1 with the true layered-earth background conductivity model. The area shown with grids defines the extent of the anomalous domain in the inversions.

dicted data at every step of the iterative inversion. The numerical study shows that, for the simple geoelectrical models considered in our paper, the MGQL method produces a very accurate result, comparable to the rigorous IE solution (Ueda and Zhdanov, 2005). At the same time, for validating of the new algorithm it is always useful to try the inversion code on the data produced by a different forward
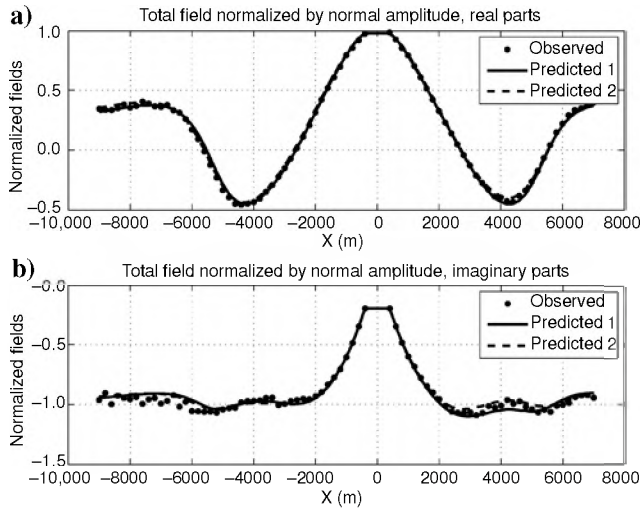

Figure 4. (a) The plots of the real and (b) imaginary parts of the normalized observed and predicted inline electric fields E_x at a frequency of 0.25 Hz for receiver 10 ($x = -1000$ m) in model 1. The dots show the noisy observed data, whereas the predicted data for a model obtained by the inversion are plotted by lines. The solid line corresponds to the predicted data (predicted 1) obtained by inversion with the true 1D background model, whereas the dashed line shows the predicted data (predicted 2) computed for 3D inversion result obtained with the background model found by 1D inversion.
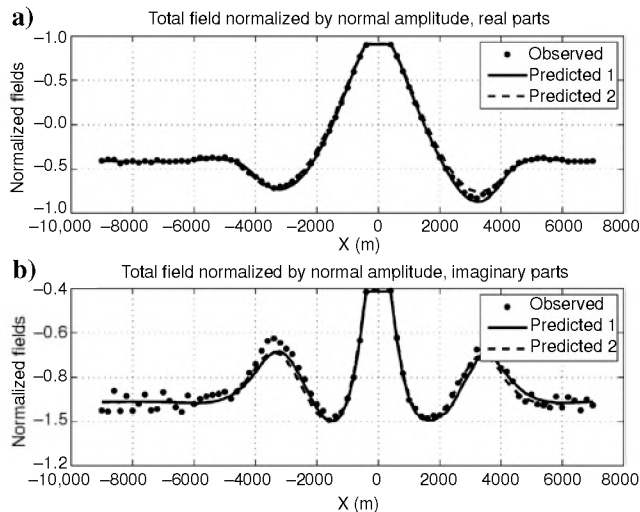
Figure 5. (a) The plots of the real and (b) imaginary parts of the normalized observed and predicted inline electric fields E_x at a frequency of 0.75 Hz for receiver 3 ($x = -1000$ m, $y = 0$ m) in model 1. The dots show the noisy observed data, whereas the predicted data for a model obtained by the inversion are plotted by lines. The solid line corresponds to the predicted data (predicted 1) obtained by inversion with the true 1D background model, whereas the dashed line shows the predicted data (predicted 2) computed for 3D inversion result obtained with the background model found by 1D inversion.

modeling method. In this case, the synthetic observed data were computed using the rigorous IE forward-modeling calculations, while in the inversion algorithm we used a MGQL approximation as the forward-modeling solver. We ran practically the same number of RRCG iterations for this data as for the noise-free data example considered above. No a priori model was used in this inversion as well. The vertical section of the resulting inverse model is shown in Figure 6. As one can see, the inversion result is still very close to the one obtained for the noise-free data with the inversion algorithm based on rigorous forward modeling. This example illustrates the stability of the method with respect to the noise in the data and modeling noise related to the different forward-modeling solvers used for synthetic observed data calculation and in the inversion algorithm.

In the previous examples, we assumed that the true 1D background conductivity model was known. We now investigate a more realistic situation where this background model is unknown. In this case, we can apply the 1D inversion to the data recorded by receivers 1 and 9, located outside of the area with two resistivity reservoirs. As a result of 1D inversion, we found the following parameters of the new 1D background model: thicknesses of the layers: 300, 100, and 1400 m and resistivities of the layers: 0.25, 5.44, 0.97, and 4.29 ohm-m

We applied the IE-based inversion algorithm to the same noisy data, as in the previous case. However, we use a new 1D background model found by 1D inversion. We ran practically the same number of RRCG iterations for this case as for the examples considered above. Figure 7 presents the vertical section of the resulting inverse model. The dashed lines in Figures 4 and 5 show the predicted data computed for the 3D inversion result obtained with the background model found by 1D inversion. One can see in these figures that the predicted data still fit the observed noisy data within the level of the noise, and the inverse model shown in Figure 7 represents a reasonable image of the targets.

This example shows that the interpretation of the practical MCSEM data should consist of two stages. In the first stage, we found the horizontally layered background geoelectrical model by 1D inversion of the observed data. In the second stage, we ran full 3D inversion using the corresponding 1D inverse model as a background.

Model 2

In the next numerical experiment, we consider a CSEM survey over a truly 3D target: a petroleum reservoir in the presence of a salt dome structure. Figures 8 and 9 show a plan view and a vertical cross section of the model. The sea-bottom reservoir is approximated by a thin resistive body located at a depth of 900 m below sea level, with a thickness of 100 m, and a horizontal size of 800×800 m. The resistivity of the reservoir is 50 ohm-m. There is located, also, an irregular-shaped salt dome structure close to the reservoir at a depth of 700 m below the sea bottom. The resistivity of the salt dome is 30 ohm-m. The depth of the sea bottom is 500 m from the surface, and the seawater resistivity is assumed to be equal to 0.25 ohm-m. The salt dome and the reservoir are surrounded by conductive sea-bottom sediments with a resistivity of 1 ohm-m. A 3D image of the true model is shown in Figure 10.

A synthetic CSEM survey consists of fourteen sea-bottom receivers and an electric dipole transmitter moving along two mutually orthogonal lines at an elevation of 50 m above the sea bottom. The positions of the receivers are shown by red dots in Figure 8. The separation between the receivers is 250 m. The locations of the transmit-

ters are shown by green diamonds in the same figure. The transmitter sends a frequency-domain EM signal with two frequencies of 0.25 and 0.75 Hz from points located every 100 m along the transmitter's line. The receivers measure the inline components of the electric field only. The observed data are computed with the rigorous IE forward-modeling code and are contaminated by random Gaussian noise, with the noise level increasing linearly from 5% at zero offset up to 10% at 3000 m offset to simulate the typical noise behavior in the field data. The area of inversion is extended from −600 to 600 m in the x-direction, from −600 to 600 m in the y-direction direction, and from 700 to 1200 m at depth. We discretize the inversion domain into 1320 Prismatic cells with the cell sizes equal to 100, 100, and 50 m in the x-, y-, and z-directions, respectively.

We have conducted two numerical experiments. In the first experiment, we have used an approach based on inhomogeneous background conductivity (Zhdanov and Wilson, 2004). We have assumed that the position of the salt dome is known, and we have included a salt dome in the inhomogeneous background. This approach seems to be quite realistic. There are practical cases of offshore geophysical exploration where the salt dome structure is known from seismic data, but the location of the petroleum reservoir is unknown. Our new inversion method makes it possible to include this known information in the background geoelectrical model. We ran the rigorous IE-based inversion and after 45 iterations we obtained a normalized weighted residual between the observed noisy data and predicted data equal to 5%. Figures 11 and 12 present the plots of the real (a) and imaginary (b) parts of the normalized observed and predicted inline electric fields E_x at a frequency of 0.25 and 0.75 Hz, respectively, at receiver 3 ($x = -250$ m, $y = 0$ m). The dots show the noisy observed data, while the predicted data for a model obtained by the inversion are plotted by lines. The solid line corresponds to the predicted data (predicted 1) obtained by inversion with the true salt dome background model. We can see that the predicted data fit the observed data very well. The corresponding inverse model is shown in Figures 13 and 14. One can see that the depth and the horizontal extent of the reservoir and its resistivity are recovered well in the inverse image. However, we can see some artificial resistive structures in the corners of the 3D inversion domain. The presence of these noisy elements in the inverse image is easily explained by the effect of the noise in the data, and by the fact that these corners of the inversion domain are located far away from the observational lines.

In the second experiment, we have assumed that we know the incorrect shape of the salt dome structure and the incorrect resistivity of 25 ohm-m. A new distorted background model of a salt dome is shown in Figure 15. We have applied the IE-based inversion to the same noisy data we used in the previous experiment. However, we used the distorted salt dome background conductivity model in the inversion. We ran the rigorous IE-based inversion with 10 smooth iterations and 30 focusing iterations. The convergence plot of the inversion process is shown in Figure 16. Note that the first iteration of

the RRCG method is computed with the regularization parameter $\alpha = 0$. There is a jump in both plots at iteration 2, because at this iteration we calculate the optimal starting value of the regularization parameter and introduce it in the inverse process. After iteration 2, the normalized residual and the parametric functional steadily decrease. After 40 iterations of the rigorous inversion, the normalized residual reaches almost 5%.
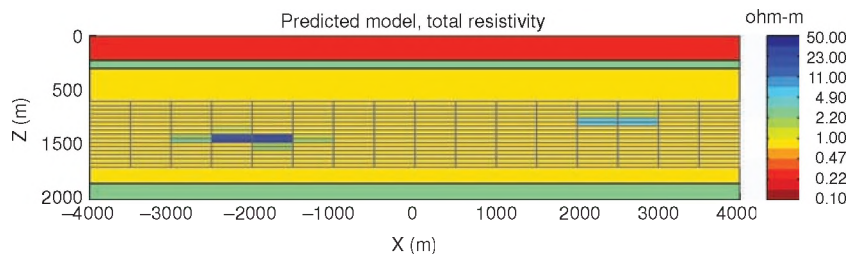

Figure 6. The vertical section of the result of the inversion of the data contaminated by random noise for model 1. The noise level increases linearly from 1% at zero offset up to 7% at 10,000 m offset. The true layered-earth background conductivity model is used in the inversion. The area shown with grids defines the extent of the anomalous domain in the inversions.
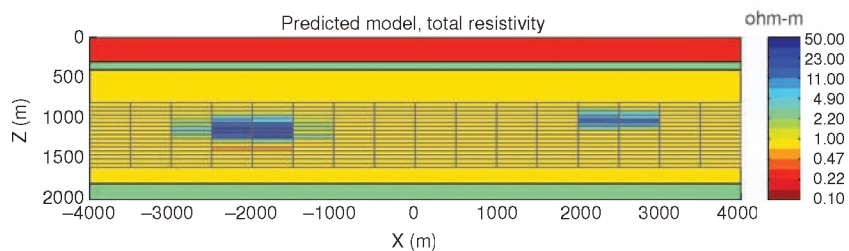

Figure 7. The vertical section of the result of the inversion of the data contaminated by random noise for model 1. The noise level increases linearly from 1% at zero offset up to 7% at 10,000 m offset. The 3D inversion result is obtained with the background model found by 1D inversion. The area shown with grids defines the extent of the anomalous domain in the inversions.
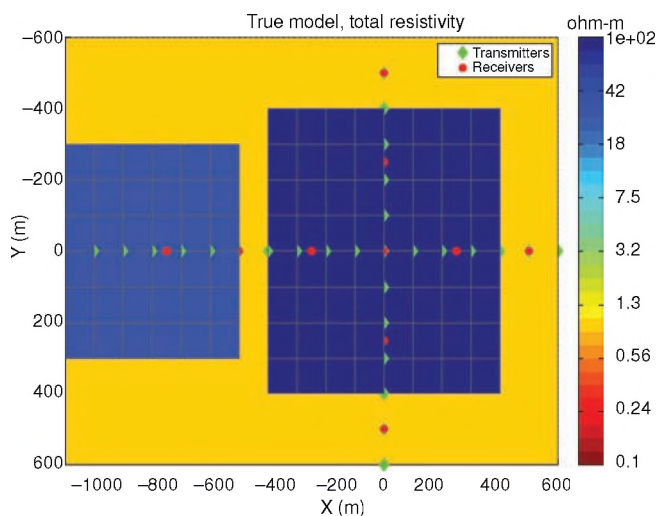

Figure 8. Model 2. A petroleum reservoir in the presence of a salt dome structure (plan view). The positions of the receivers are shown by red dots, whereas the green diamonds show the transmitters locations.
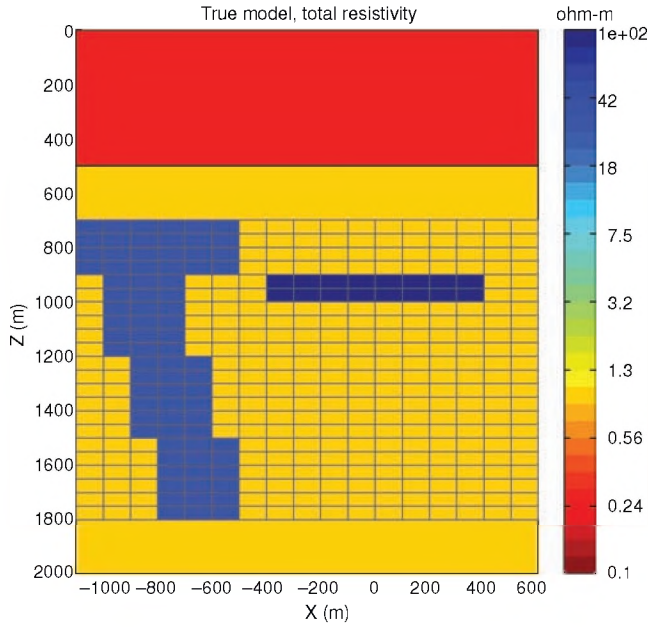
Figure 9. Model 2. A petroleum reservoir in the presence of a salt dome structure (vertical section). The area shown with grids defines the extent of the anomalous domain in the inversions.
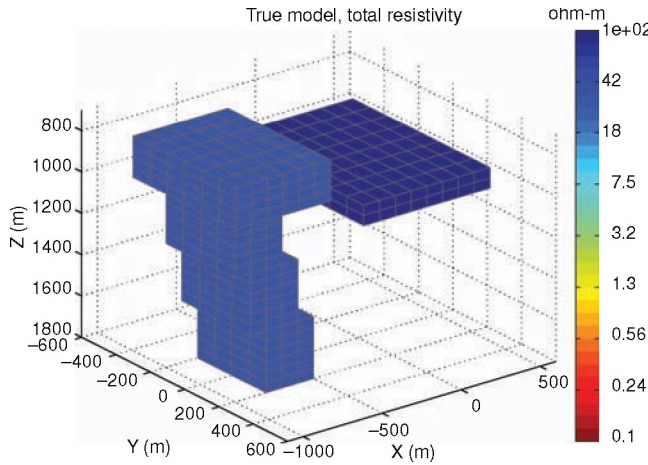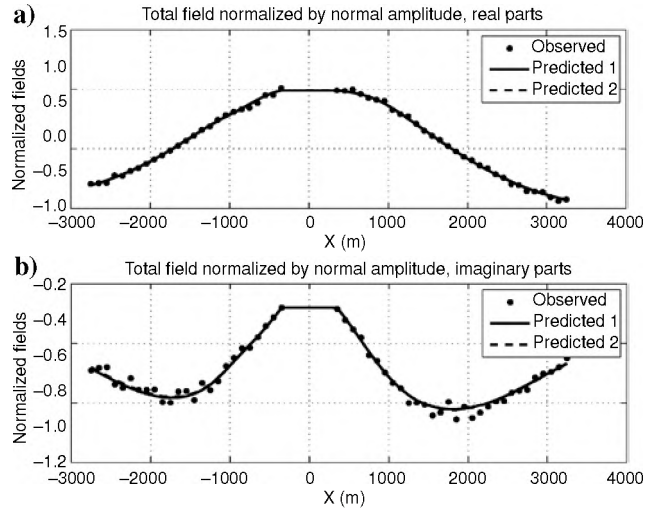

Figure 11. The plots of the (a) real and (b) imaginary parts of the normalized observed and predicted inline electric fields E_x at a frequency of 0.25 Hz for receiver 3 ($x = -250$ m, $y = 0$ m) in model 2. The dots show the noisy observed data, whereas the predicted data for a model obtained by the inversion are plotted by blue lines. The solid line corresponds to the predicted data (predicted 1) obtained by inversion with the true salt dome background model, whereas the dashed line shows the predicted data (predicted 2) computed for 3D inversion result obtained with the distorted background model of a salt dome.
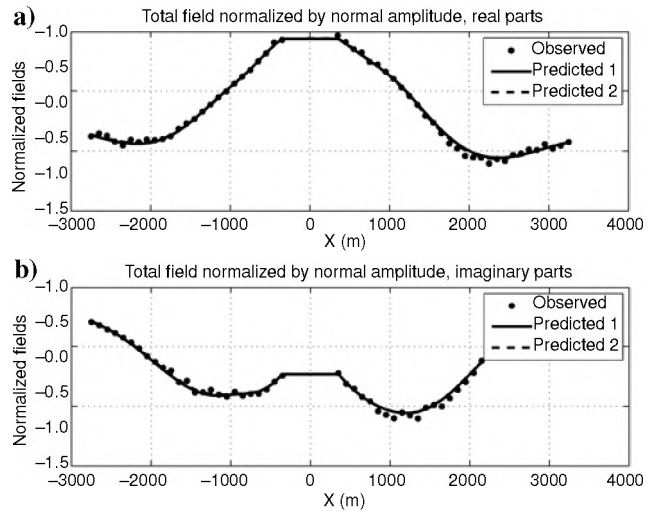

Figure 10. A 3D image of true Model 2.

Figure 12. The plots of the (a) real and (b) imaginary parts of the normalized observed and predicted inline electric fields E_x at a frequency of 0.75 Hz for receiver 3 ($x = -250$ m, $y = 0$ m) in model 2. The dots show the noisy observed data, whereas the predicted data for a model obtained by the inversion are plotted by lines. The solid line corresponds to the predicted data (predicted 1) obtained by inversion with the true salt dome background model, whereas the dashed line shows the predicted data (predicted 2) computed for 3D inversion result obtained with the distorted background model of a salt dome.

Figure 17 shows the vertical section of the result of the inversion, while Figure 18 presents the corresponding 3D image of the inverse model. We still can clearly see the resistive reservoir in these figures. However, the images are slightly distorted due to incorrect selection of the background model. This result demonstrates that even in the case of the inaccurate information about the background model, the inversion is still able to recover the meaningful image of the resistive reservoir.
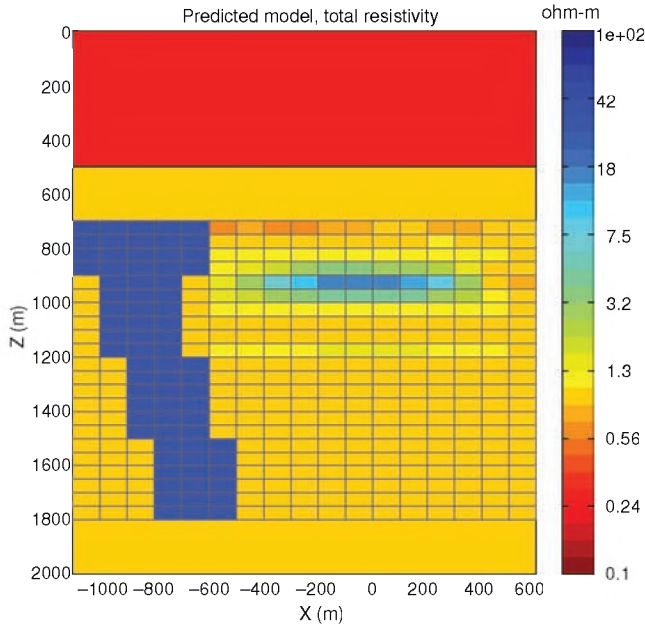

Figure 13. The vertical section of the result of the inversion of the data contaminated by random noise for model 2. The noise level increases linearly from 5% at zero offset up to 10% at 3000 m offset. The true salt dome background conductivity model is used in the inversion. The area shown with grids defines the extent of the anomalous domain in the inversions.
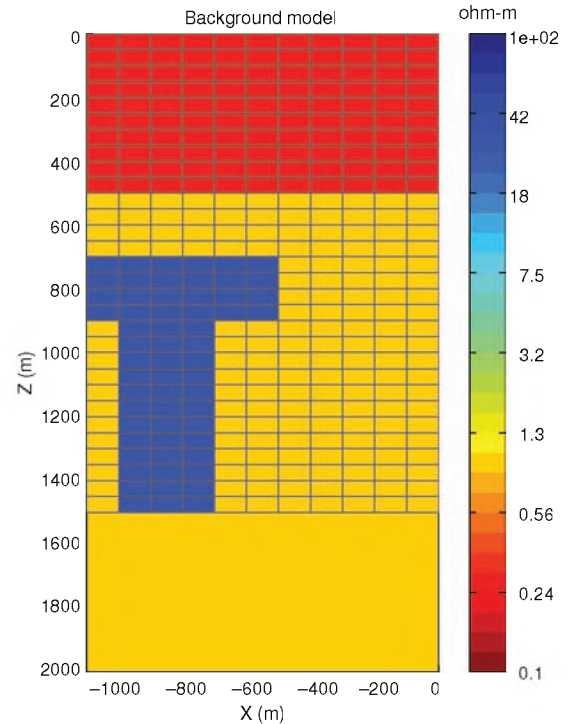

Figure 15. A vertical section of the distorted background model of a salt dome. The area shown with grids defines the extent of the anomalous domain in the inversions.
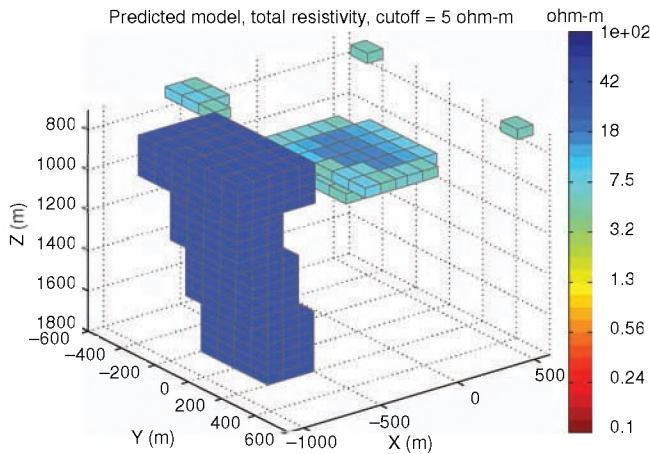

Figure 14. A 3D image of the result of the inversion of the data contaminated by random noise for model 2. The true salt dome background conductivity model is used in the inversion.
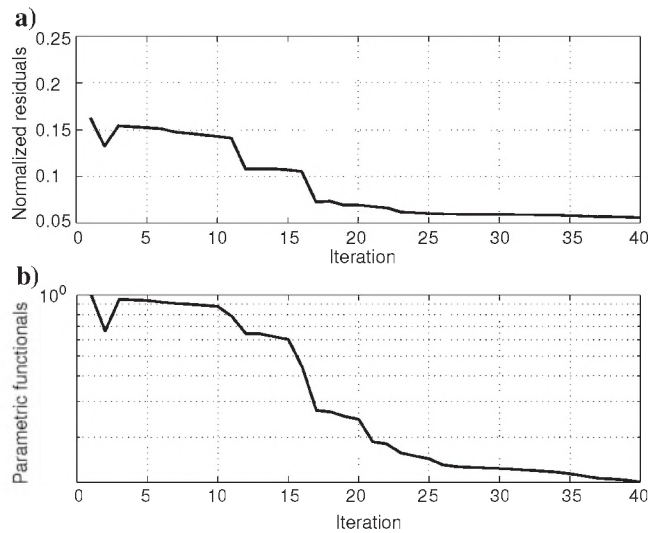

Figure 16. The convergence plots of the iterative inversion for Model 2 with the data contaminated by random noise. The noise level increases linearly from 5% at zero offset up to 10% at 3000 m offset. (a) The normalized residual versus the iteration number, (b) the normalized parametric functional behavior. The distorted salt dome background conductivity model is used in the inversion.
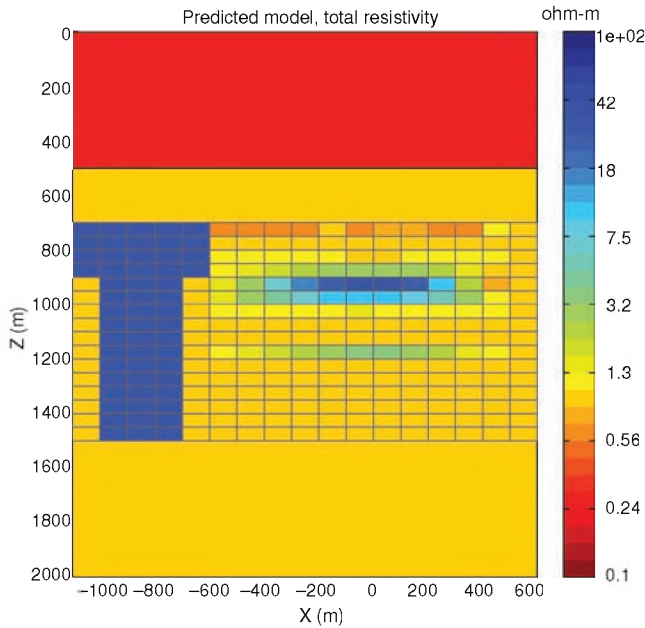
Figure 17. The vertical section of the result of the inversion of the data contaminated by random noise for model 2. The noise level increases linearly from 5% at zero offset up to 10% at 3000 m offset. The distorted salt dome background conductivity model is used in the inversion.
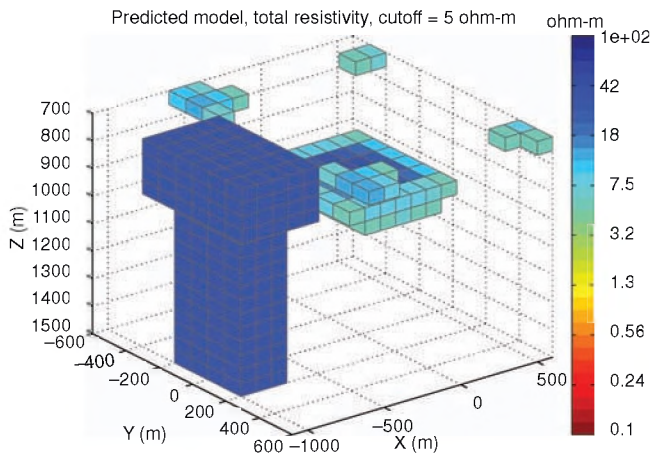

Figure 18. A 3D image of the result of the inversion of the data contaminated by random noise. The distorted salt dome background conductivity model is used in the inversion.

CONCLUSIONS

We developed a rigorous method for 3D inversion of MCSEM data based on the integral equation formulation. The paper presents a theoretical background of this new method and a numerical proof of concept. We tested this method on a relatively simple synthetic 2D CSEM survey, simulating the typical transmitter-receiver layout which is currently used by EM-acquisition companies. The results of these tests demonstrate that the inverse images generated by this method provide a reasonable reconstruction of the true location and the resistivity of the target. We show also that this method has the potential to be used for full 3D inversion of the MCSEM data collected by 3D surveys. We have illustrated the theory and the corresponding numerical methods by simple, but meaningful numerical examples, because practical experience shows that the most effective way to test the new method and computer code is by analyzing relatively simple models. At the same time, our models may serve as a good testing ground for a comparison of different inversion codes in the future.

We should note that the IE method does not necessarily require a small inversion domain. The inversion area can be as large as necessary. However, if there is any a priori information available about the known geologic structures, this information may be included in the background model. The only difference between say, the FD solution and the IE-based solution is that in the first case one should use the corresponding boundary conditions and include in the modeling grid, the cells located very far away from the true area of potential target location. In the framework of the IE approach, we assume that the background model is known inside and/or outside of the inversion area, and we focus our inversion on the potential target. The last property of the IE technique is beneficial because it allows more inversion cells to be used to describe the fine structure of the area of investigation, while in the FD approach many inversion cells are located at a large distance from the target area, including the air and the water layers.

A serial version of the code can be run on a single PC. The typical inversion on a grid of up to a few thousand inversion cells requires just less than half an hour of computational time on an AMD 4400 + (2.2 GHz) 3.25 GB of RAM Windows PC.

We should conclude that there is still a lot of work ahead to make this method a practical tool for MCSEM data interpretation for offshore petroleum exploration. For example, we are working now on a parallel version of the code based on our new parallel IE-modeling software PIE3D. The parallel version will allow us to consider large-scale inverse problems and use large inversion domains with the inhomogeneous background to represent the true complexity of sea-bottom geoelectrical structures. Future research will be directed to the analysis of more complex geoelectrical models and to application of the developed method for interpretation of field MCSEM data.

APPENDIX A

QUASI-ANALYTICAL APPROXIMATION FOR A VARIABLE BACKGROUND (QAVB)

Zhdanov and Wilson (2004) introduced a new formulation of the QA approximation which can be used for models with a 3D arbitrary, or inhomogeneous, background conductivity distribution. This approximation was used by Golubev and Zhdanov (2005) to develop a modified QA expression for both the forward modeling and for the Fréchet derivative computation in magnetotelluric (MT) inverse problem solution. In the current paper, we introduce a new improved formulation of the QA approximation for models with variable backgrounds, which results in more accurate integral representation for the Fréchet derivative as well.

Following Zhdanov et al. (2006), we assume now that the conductivity within a 3D geoelectrical model can be represented by the normal (horizontally layered) conductivity σ_{norm}, background conductivity $\sigma_b = \sigma_{\text{norm}} + \Delta\sigma_b$, and an arbitrarily varying conductivity $\sigma = \sigma_b + \Delta\sigma_a$, within a domain D.

In this model, the electromagnetic field can be presented as a sum of the background field, $\mathbf{E}^b$, $\mathbf{H}^b$, and the anomalous field, $\mathbf{E}^{\Delta\sigma_a}$, $\mathbf{H}^{\Delta\sigma_a}$:

$$\mathbf{E} = \mathbf{E}^b + \mathbf{E}^{\Delta\sigma_a}, \quad \mathbf{H} = \mathbf{H}^b + \mathbf{H}^{\Delta\sigma_a}, \quad \text{(A-1)}$$

where the background field is a field generated by the given sources in the model with a background distribution of conductivity σ_b, and the anomalous field is produced by the anomalous conductivity distribution $\Delta\sigma_a$:

$$\mathbf{E}^{\Delta\sigma_a}(\mathbf{r}_j) = \mathbf{E}(\mathbf{r}_j) - \mathbf{E}^n(\mathbf{r}_j) - \mathbf{E}^{\Delta\sigma_b}(\mathbf{r}_j) = \mathbf{G}_E(\Delta\sigma_a\mathbf{E}),$$

$$\text{(A-2)}$$

$$\mathbf{H}^{\Delta\sigma_a}(\mathbf{r}_j) = \mathbf{H}(\mathbf{r}_j) - \mathbf{H}^n(\mathbf{r}_j) - \mathbf{H}^{\Delta\sigma_{ab}}(\mathbf{r}_j) = \mathbf{G}_H(\Delta\sigma_a\mathbf{E}).$$

$$\text{(A-3)}$$

Note that formulas A-2 and A-3 can be rewritten in the form:

$$\mathbf{E}^{\Delta\sigma_a}(\mathbf{r}_j) = \mathbf{G}_E(\Delta\sigma_a(\mathbf{E}^b + \mathbf{E}^{\Delta\sigma_a})), \quad \text{(A-4)}$$

$$\mathbf{H}^{\Delta\sigma_a}(\mathbf{r}_j) = \mathbf{G}_H(\Delta\sigma_a(\mathbf{E}^b + \mathbf{E}^{\Delta\sigma_a})). \quad \text{(A-5)}$$

Following the main ideas of the QL approximation, we assume that inside the local inhomogeneity D, the anomalous field $\mathbf{E}^{\Delta\sigma_a}$ is linearly proportional to the background electric field $\mathbf{E}^b$:

$$\mathbf{E}^a = \mathbf{E}^{\Delta\sigma_a} = \hat{\boldsymbol{\lambda}}_a \cdot \mathbf{E}^b. \quad \text{(A-6)}$$

Substituting A-6 into A-4 and A-5, we arrive at the QL approximation of the anomalous electromagnetic field for a model with a variable background conductivity (QLVB approximation):

$$\mathbf{E}^{\Delta\sigma_a} \approx \mathbf{E}^{QLVB} = \mathbf{G}_E[\Delta\sigma_a(\hat{\mathbf{I}} + \hat{\boldsymbol{\lambda}}_a) \cdot \mathbf{E}^b], \quad \text{(A-7)}$$

$$\mathbf{H}^{\Delta\sigma_a} \approx \mathbf{H}^{QLVB} = \mathbf{G}_H[\Delta\sigma_a(\hat{\mathbf{I}} + \hat{\boldsymbol{\lambda}}_a) \cdot \mathbf{E}^b]. \quad \text{(A-8)}$$

Therefore, we have the following equation for $\hat{\boldsymbol{\lambda}}_a$:

$$\hat{\boldsymbol{\lambda}}_a \cdot \mathbf{E}^b = \mathbf{G}_E[\Delta\sigma_a(\hat{\mathbf{I}} + \hat{\boldsymbol{\lambda}}_a) \cdot \mathbf{E}^b]. \quad \text{(A-9)}$$

In the framework of the quasi-linear approach, the electrical reflectivity tensor can be selected to be a scalar: $\hat{\boldsymbol{\lambda}}_a = \lambda_a$. In this case, integral formula A-9 can be cast in the form:

$$\lambda_a(\mathbf{r}_j)\mathbf{E}^b(\mathbf{r}_j) = \mathbf{G}_E[\Delta\sigma_a\lambda_a\mathbf{E}^b] + \mathbf{E}^Q(\mathbf{r}_j), \quad \text{(A-10)}$$

where $\mathbf{E}^Q$ is the quasi-Born approximation of the anomalous field. We call this term a quasi-Born approximation, because in the case of the conventional Born approximation, one should use the normal electric field inside the Green's operator:

$$\mathbf{E}^Q = \mathbf{G}_E[\Delta\sigma_a\mathbf{E}^b].$$

Following the ideas of the original QA approximation, we use the fact that the Green's tensor $\hat{\mathbf{G}}_E(\mathbf{r}_j|\mathbf{r})$ exhibits either singularity or a peak at the point where $\mathbf{r}_j = \mathbf{r}$. Therefore, one can expect that the dominant contribution to the integral $\mathbf{G}_E[\Delta\sigma_a\lambda\mathbf{E}^b]$ in equation A-10 is from some vicinity of the point $\mathbf{r}_j = \mathbf{r}$. Assuming also that $\lambda_a(\mathbf{r})$ is slowly varying within domain D, one can write

$$\lambda_a(\mathbf{r}_j)\mathbf{E}^b(\mathbf{r}_j) \approx \lambda_a(\mathbf{r}_j)\mathbf{G}_E[\Delta\sigma_a\mathbf{E}^b] + \mathbf{E}^Q(\mathbf{r}_j)$$

$$= \lambda_a(\mathbf{r}_j)\mathbf{E}^Q(\mathbf{r}_j) + \mathbf{E}^Q(\mathbf{r}_j). \quad \text{(A-11)}$$

Note that expression A-11 represents a vector equation, while we have just one scalar unknown function, $\lambda_a(\mathbf{r}_j)$. Taking into account that we are looking for a scalar reflectivity tensor, it is useful to introduce a scalar equation based on the vector equation A-11. We can obtain a scalar equation by taking the scalar product of both sides of equation A-11 with the complex conjugate background electric field:

$$\lambda_a(\mathbf{r}_j)\mathbf{E}^b(\mathbf{r}_j) \cdot \mathbf{E}^{b*}(\mathbf{r}_j) = \lambda_a(\mathbf{r}_j)\mathbf{E}^Q(\mathbf{r}_j) \cdot \mathbf{E}^{b*}(\mathbf{r}_j)$$

$$+ \mathbf{E}^Q(\mathbf{r}_j) \cdot \mathbf{E}^{b*}(\mathbf{r}_j). \quad \text{(A-12)}$$

Dividing equation A-12 by the square of the normal field and assuming that

$$\mathbf{E}^b(\mathbf{r}_j) \cdot \mathbf{E}^{b*}(\mathbf{r}_j) \neq 0, \quad \text{(A-13)}$$

we obtain

$$\lambda_a(\mathbf{r}_j) = \lambda_a(\mathbf{r}_j)g^Q(\mathbf{r}_j) + g^Q(\mathbf{r}_j), \quad \text{(A-14)}$$

where:

$$g^Q(\mathbf{r}_j) = \frac{\mathbf{E}^Q(\mathbf{r}_j) \cdot \mathbf{E}^{b*}(\mathbf{r}_j)}{\mathbf{E}^b(\mathbf{r}_j) \cdot \mathbf{E}^{b*}(\mathbf{r}_j)}.$$

Solving equation A-14, we find

$$\lambda_a(\mathbf{r}_j) = \frac{g^Q(\mathbf{r}_j)}{1 - g^Q(\mathbf{r}_j)}. \quad \text{(A-15)}$$

Note that at the points where the background field vanishes, we can select λ_a equal to (-1):

$$\lambda_a(\mathbf{r}_j) = -1, \quad \text{if } \mathbf{E}^b(\mathbf{r}_j) \cdot \mathbf{E}^{b*}(\mathbf{r}_j) = 0.$$

Substituting equation A-15 into A-1, we find

$$\mathbf{E}(\mathbf{r}) \approx [\lambda_a(\mathbf{r}) + 1]\mathbf{E}^b(\mathbf{r}) = \frac{1}{1 - g^Q(\mathbf{r})}\mathbf{E}^b(\mathbf{r}).$$

$$\text{(A-16)}$$

Therefore, from equations A-2 and A-3, we finally determine

$$\mathbf{E}_{QAVB}^{\Delta\sigma_a}(\mathbf{r}_j) = \int\int\int_D \hat{\mathbf{G}}_E(\mathbf{r}_j|\mathbf{r}) \cdot \left[\frac{\Delta\sigma_a(\mathbf{r})}{1 - g^Q(\mathbf{r})} \mathbf{E}^b(\mathbf{r}) \right] dv,$$

$$(\text{A-17})$$

and

$$\mathbf{H}_{QAVB}^{\Delta\sigma_a}(\mathbf{r}_j) = \int\int\int_D \hat{\mathbf{G}}_H(\mathbf{r}_j|\mathbf{r}) \cdot \left[\frac{\Delta\sigma_a(\mathbf{r})}{1 - g^Q(\mathbf{r})} \mathbf{E}^b(\mathbf{r}) \right] dv.$$

$$(\text{A-18})$$

Equations A-17 and A-18 give quasi-analytical solutions with the variable background (QAVB) for 3D electromagnetic fields. We should note that formulas A-17 and A-18 provide more accurate approximations of the anomalous field than the original QA approximations developed by Zhdanov et al. (2000), because they are based on the linear relationship between the anomalous and the background fields, while the original approximations used a similar relationship between the anomalous and the normal fields. In the case of the high conductivity contrast between the inhomogeneity and the horizontally layered background, the accuracy of the original QL and QA approximations may decrease, while using the appropriate variable background model can make this approximation as close to the true data as required.

REFERENCES

Carazzone, J. J., O. M. Burtz, K. E. Green, and D. A. Pavlov, 2005, Three dimensional imaging of marine CSEM data: 75th Annual International Meeting, SEG, Expanded Abstracts, 575–578.

Eidesmo, T., S. Ellingsrud, L. M. MacGregor, S. Constable, M. C. Sinha, S. Johansen, F. N. Kong, and H. Westerdahl, 2002, Sea bed logging (SBL), a new method for remote and direct identification of hydrocarbon filled layers in deepwater areas: First Break, **20**, 144–152.

Ellingsrud, S., T. Eidesmo, and S. Johansen, 2002, Remote sensing of hydrocarbon layers by seabed logging (SBL): Results from a cruise offshore Angola: The Leading Edge, **21**, 972–982.

Golubev, N., and M. S. Zhdanov, 2005, Accelerated integral equation inversion of 3D magnetotelluric data in models with inhomogeneous background: 75th Annual International Meeting, SEG, Expanded Abstracts, 530–533.

Hesthammer, J., and M. Boulaenko, 2005, The offshore EM challenge: First Break, **23**, 59–66.

Hoversten, G. M., F. Cassassuce, and G. A. Newman, 2004, Direct reservoir parameter estimation using joint inversion of seismic AVO and marine CSEM data: 74th Annual International Meeting, SEG, Expanded Abstracts, 1507–1510.

Hoversten, G. M., J. Chen, E. Gasperikova, and G. A. Newman, 2005, Integration of marine CSEM and seismic AVA data for reservoir parameter estimation: 75th Annual International Meeting, SEG, Expanded Abstracts, 579–582.

Newman, G. A., and P. T. Boggs, 2004, Solution accelerators for large-scale threedimensional electromagnetic inverse problems: Inverse Problems, **20**, S151–S170.

Portniaguine, O., and M. S. Zhdanov, 1999, Focusing geophysical inversion images: Geophysics, **64**, 874–887.

Srnka, L. J., J. J. Carazzone, E. A. Eriksen, and M. S. Ephron, 2005, Remote reservoir resistivity mapping — An overview: 75th Annual International Meeting, SEG, Expanded Abstracts, 569–571.

Tikhonov, A. N., and V. Y. Arsenin, 1977, Solution of ill-posed problems: V. H. Winston and Sons.

Tompkins, M. J., 2004, Marine controlled-source electromagnetic imaging for hydrocarbon exploration: Interpreting subsurface electrical properties: First Break, **22**, 45–51.

Ueda, T., and M. S. Zhdanov, 2005, Fast numerical modeling of multitransmitter electromagnetic data using multigrid quasi-linear approximation: IEEE Transactions on Geoscience and Remote Sensing, **44**, 1428–1434.

Zhdanov, M. S., 2002, Geophysical inverse theory and regularization problems: Elsevier Science Publ. Co., Inc.

Zhdanov, M. S., L. Cox, A. Gribenko, and G. A. Wilson, 2006, Controlled source electromagnetic inversion using quasi-analytical approximation with variable background: Proceedings of the Annual Meeting, Consortium for Electromagnetic Modeling and Inversion, 83–102.

Zhdanov, M. S., V. I. Dmitriev, S. Fang, and G. Hursán, 2000, Quasi-analytical approximations and series in electromagnetic modeling: Geophysics, **65**, 1746–1757.

Zhdanov, M. S., and G. Hursán, 2000, 3D electromagnetic inversion based on quasi-analytical approximation: Inverse Problems, **16**, 1297–1322.

Zhdanov, M. S., and E. Tolstaya, 2004, Minimum support nonlinear parameterization in the solution of 3-D magnetotelluric inverse problem: Inverse Problems, **20**, 937–952.

Zhdanov, M. S., and G. A. Wilson, 2004, 3D Quasi-analytical inversion of electromagnetic fields in the models with inhomogeneous background: 74th Annual International Meeting, SEG, Expanded Abstracts, 692–695.